An electrochromic corundum-like compound based on the reversible (de)insertion of lithium: Li2Ni2W2O9

Simon Redor, Louis Godeffroy, Gwenaëlle Rousse, Artem Abakumov, Biao Li, Frédéric Kanoufi, Jean-Marie Tarascon

To cite this version:

Simon Redor, Louis Godeffroy, Gwenaëlle Rousse, Artem Abakumov, Biao Li, et al.. An electrochromic corundum-like compound based on the reversible (de)insertion of lithium: Li2Ni2W2O9. Journal of the American Chemical Society, 2023, 145 (23), pp.12823-12836. 10.1021/jacs.3c03631 . hal-04237601

HAL Id: hal-04237601
https://hal.science/hal-04237601
Submitted on 11 Oct 2023

An electrochromic corundum-like compound based on the reversible (de)insertion of lithium: $Li_2Ni_2W_2O_9$

Authors: Simon Redor[1,2], Louis Godeffroy[3], Gwenaëlle Rousse[1,2], Artem M. Abakumov[4], Biao Li[5], Frédéric Kanoufi[3], and Jean-Marie Tarascon[1,] *

Institution adress: Chaire de Chimie du Solide et de l'Energie, UMR 8260, Collège de France, 75231, Cedex 05 Paris, France.

Affiliations:

1 – Chaire de Chimie du Solide et de l'Energie, UMR 8260, Collège de France, 75231, Cedex 05 Paris, France.

2 – Sorbonne Université, F-75005, Paris, France

3 – ITODYS, UMR 7086, Universite Paris Cité, 75013, Paris, France.

4 – Center for Electrochemical Energy Storage, Skolkovo Institute of Science and Technology, Moscow 143026, Russia

5 – School of Materials Science and Engineering, Peking University, Beijing 100871, P. R. China

Abstract

The search for efficient anodic electrochromic materials is essential to the development of electrochromic devices, such as smart windows. Magnetron-sputtered lithium-nickel-tungsten mixed oxides are good candidates to tackle this issue; however, they display a complicated microstructure, making it difficult to pinpoint the origin of their electro-optical properties. Herein, by exploring the Li_2O-NiO-WO_3 phase diagram, we obtained a new phase, $Li_2Ni_2W_2O_9$, that crystallizes in the orthorhombic *Pbcn* space group. This material can reversibly uptake/release 0.75 Li^+ (31 $mAh.g^{-1}$) when cycled between 2.5 and 5.0 V vs Li^+/Li. Moreover, through *operando* optical microscopy, we show that this new phase is electrochromic, and access crucial information about the diffusion-limited insertion of lithium at the single-particle-scale. This study sets the ground for future syntheses of electrochemically active materials crystallizing in the ramsayite structure, and details how the electrochromic properties of battery materials can be used to shed some light on their electrochemical mechanisms.

Introduction

Electrochromic materials are characterized by a reversible and persistent change of optical properties when they are exposed to an externally applied voltage. This property has been popularized in the 1960s[1,2], and today, these electrochromic materials are used to develop electrochromic devices: these optical devices can go from a fully transparent state to a darker, colored state, and are mostly studied for their application to self-dimming mirrors and glasses, electrochromic displays and smart windows[3,4]. The latter are a key technology as they can make our buildings more energy-efficient, by screening specific wavelengths from solar emissions, especially infrared wavelengths[5,6].

An electrochromic device is usually composed of two electrodes, each deposited on their own transparent conductive oxide thin film, and separated by a transparent solid electrolyte. The coloration/bleaching process of the device comes from the rocking of small cations (H^+, Li^+, Na^+…) from one electrode to the other, driven by an external voltage bias. A WO_3 thin film is often used as the working electrode, due to the material's great performances and a good understanding of its structure and properties[7,8]. The material used as the counter electrode in the device can vary, but NiO thin films are a common choice. However, electrochromic NiO thin films are plagued by two issues: low transmittance modulation between the bleached and the colored states, and poor cycling stability[9–11].

An interesting method used to solve these issues is to mix NiO with other cations in thin films. Mixing NiO with lithium has been shown to increase the optical modulation of the material[12,13], while mixing with heavy cations like W(VI) can improve the durability of the film[14,15]. However, few reports were made on Li-Ni-W oxide thin films: Lin *et al.* discussed the electrochromic properties of a radio-frequency (rf) magnetron sputtered $Li_{1.81}NiW_{0.21}O_x$ thin film[16], while Gillaspie *et al.* reported the performances of a $Li_{1.2}NiW_{0.1}O_x$ film, that was also prepared through rf magnetron sputtering[17]. In both cases, the cationic mixing improved the optical modulation and the durability of the films compared to pure NiO. Another interesting aspect of these two compositions is the morphology of the films: both of them were nanocomposites, with cubic rocksalt NiO nanocrystallites embedded in an amorphous matrix. The matrix supposedly improved the diffusion of lithium cations to the crystallites, which was one of the reasons proposed for the good performances of these nanocomposites[16].

In these two cases, tungsten is only used as a doping agent in order to create the unique microstructure of the films, and it might be argued that the "electrochromic components" of these materials are only the NiO nanocrystallites. However, there have been reports on monophasic crystallized Li-Ni-W mixed oxides, able to reversibly insert Li^+ cations: the triclinic $Li_2Ni(WO_4)_2$ phase[18,19], as well as $Li_{4+x}Ni_{1-x}WO_6$ phases[20]. The electrochromic properties of these phases have yet to be studied; nonetheless, since they contain the two transition metals most associated with electrochromism, chances are high that these mixed oxides are also electrochromic. In the case of $Li_2Ni(WO_4)_2$, cathodic electrochromism would be expected as its lithiation process is associated with the W^{6+}/W^{5+} redox couple. Meanwhile, for the $Li_{4+x}Ni_{1-x}WO_6$ phases, as Ni^{3+}/Ni^{2+} redox is involved in its delithiation process, anodic electrochromism would be observed. This raises the question of what these crystallized structures can bring to the field of electrochromic Li-Ni-W mixed oxides.

In this report, we present a new phase discovered during our exploration of the Li-Ni-W-O system. This phase, with the general formula $Li_2Ni_2W_2O_9$, was obtained through solid-state synthesis. It displays reversible electrochemical activity associated to the Ni^{3+}/Ni^{2+} redox couple when cycled against lithium metal at high potentials. Moreover, anodic electrochromism is clearly established thanks to *operando* optical microscopy operated at the single-particle-level[21–31].

Experimental methods

Reagents – $Li_2Ni_2W_2O_9$ powder was synthetized from nickel oxide powder (NiO, Sigma-Aldrich, 99 %), tungsten trioxide powder (WO_3, Alfa Aesar, 99.8 %), and lithium carbonate powder (Li_2CO_3, Sigma-Aldrich, ≥ 99.0 %). The $Li_2Ni_2W_2O_9$ self-standing film was made from the prepared $Li_2Ni_2W_2O_9$ powder, carbon black Super P (C, Alfa Aesar, ≥ 99 %), and a 60 wt% polytetrafluoroethylene dispersion in water (PTFE, Sigma-Aldrich).

Synthesis – $Li_2Ni_2W_2O_9$ was obtained through solid-state synthesis. For a typical batch of 2 g, NiO powder (435 mg, 2 eq.), WO_3 powder (1350 mg, 2 eq.), and Li_2CO_3 powder (215 mg, 1 eq.) were hand-ground together in an agate mortar; acetone was used to ensure an homogeneous mix. The mix was then ground for 30 minutes in a stainless steel jar containing two stainless steel balls using a SPEX SamplePrep 8000M Mixer/Mill. The resulting mix was then poured in an alumina crucible and heated in a Carbolite CWF 1200 muffle furnace. It was first heated in air at 650 °C (heating rate: 5 °C/min) for 12 h to ensure the decarbonatation of Li_2CO_3, then to 700 °C (heating rate: 2 °C/min) for 24 h. The resulting powder was ball milled for 30 minutes and was then heated again at 700 °C in air (heating rate: 5 °C/min) for 24 h, yielding a green powder.

Structural characterization – Synchrotron powder X-ray diffraction experiments (PXRD) were performed at the 11-BM beamline of the Advanced Photon Source (APS) (λ = 0.45898 Å), at Argonne National Laboratory, USA[32]. The measurements were realized in transmission mode. The $Li_2Ni_2W_2O_9$ powder was mixed with crushed glass (1:1 volume ratio) to decrease the absorption of the X-ray beam by tungsten. The samples were poured in borosilicate capillaries (0.7 mm in diameter), and sealed in Kapton tubes.

Neutron powder diffraction patterns were obtained from the Echidna diffractometer[33] (λ = 1.6220 Å) at the Open Pool Australian Lightwater (OPAL) reactor of Australia's Nuclear Science and Technology Organisation (ANSTO). The measurements were performed at room temperature using roughly 2 g of pristine $Li_2Ni_2W_2O_9$ powder placed in a vanadium cylindrical can.

All powder diffraction patterns were refined following the Rietveld method[34], in the FullProf software suite[35].

Samples for the transmission electron microscopy (TEM) were prepared by grinding the powder in an agate mortar with methanol and depositing drops of the resulting suspension on a copper TEM grid with a holey carbon layer. Electron diffraction patterns (ED), high-angle annular dark field scanning transmission electron microscopy (HAADF-STEM) images, and energy dispersive X-ray spectra in STEM-mode (STEM-EDX) were collected with a probe-corrected Titan Themis Z electron microscope operated at 200 kV and equipped with a Super-X EDX detector.

Electrochemistry – Galvanostatic charge-discharge experiments were performed using coin cells in a two-electrode setup. The working electrode was $Li_2Ni_2W_2O_9$ mixed with carbon black Super P (20 wt%), and the counter electrode was lithium metal. Aluminum foil and a stainless steel plate were used as current collectors at the positive and negative electrodes, respectively. Two layers of Whatman GF/D glass fiber filters were used as separator between the two electrodes. The electrolyte was a 1 M solution of lithium hexafluorophosphate ($LiPF_6$) in a 1:1:4 vol% mix of ethylene carbonate (EC), propylene carbonate (PC) and dimetyl carbonate (DMC).

The measurements were carried out using a BioLogic BCS-805 battery cycler, and the data was acquired using EC-Lab. The cells were cycled between 2.5 and 5.0 V vs Li^+/Li, at a current density of 10 $mA.g^{-1}$, at room temperature. Three coin cells were cycled in the same conditions to verify the repeatability of the electrochemical behavior, and to get some statistical dispersion on these measurements.

X-ray Absorption Spectroscopy (XAS) – XAS measurements were performed at the ROCK beamline[36] of SOLEIL synchrotron (France). A Si (111) quick-XAS monochromator with an oscillation frequency of 2 Hz was used to select the incident energy across the Ni K-edge. The quick-XAS spectra were collected in transmission mode using a Ni foil to ensure the energy calibration, and averaged over 10 minutes.

Samples were prepared by mixing 3 mg of active material with cellulose and pressing the resulting powder into 5-mm-wide pellet. In the case of electrochemically (de)lithiated materials, those were retrieved as quickly as possible from their electrochemical cells after cycling, centrifugated three time in clean DMC (6000 rpm, 2 minutes) and dried in vacuum, before being pressed into pellets inside an argon-filled glovebox. The resulting pellets were sealed in plastic film to avoid air exposure upon XAS measurements. The energy calibration and normalization of the XAS data was performed using DEMETER package[37]. The k^2-weighted EXAFS oscillations were extracted at Ni K-edge using a sine windows in the k-range of [2.2-16.3] $Å^{-1}$ and the refinement was done in the R-range of [1,3.25] Å. The E_0, S_0^2 and coordination number N_i were kept fixed, only the radial distance R_i and the mean-square relative displacements σ_i^2 were allowed to vary. To refine the EXAFS oscillations, we have used the starting model obtained by the structure reported in Table 1. The refined structural parameters obtained by EXAFS analysis are reported in Table S1.

Operando *XRD* – *Operando* XRD measurements were performed in a reflection mode by using $Li_2Ni_2W_2O_9$ powder mixed with carbon black Super P (20 wt%) as the working electrode in a specialized operando cell, sealed with a Be window (Figure S1). The counter-electrode was metallic lithium. Thin Al foil (thickness: 0.003 mm) and a stainless steel plate were used as current collectors at the positive and negative electrodes, respectively. Two layers of Whatman GF/D glass fiber filters were used as separators between the two electrodes. The electrolyte was a 1 M solution of lithium hexafluorophosphate ($LiPF_6$) in a 1:1:4 vol% mix of ethylene carbonate (EC), propylene carbonate (PC) and dimetyl carbonate (DMC). The cell was cycled between 2.5 and 5.0 V vs Li^+/Li, at a current density of 10 $mA.g^{-1}$, at room temperature. Electrochemical measurements were carried out using a BioLogic SP-50 potentiostat, and the electrochemical data was collected with EC-Lab.

The XRD scans were performed with a Bruker D8 Advance lab diffractometer, equipped with a Cu Kα source (λ_1 = 1.54056 Å and λ_2 = 1.54439 Å) and a LynxEye-2 detector. The measurements were performed in reflection mode, in the Bragg-Brentano configuration.

***Optical microscopy* –** *Operando* optical microscopy measurements were performed by using a $Li_2Ni_2W_2O_9$ self-standing film as a working electrode in an ECC-Opto-Std optical test cell from EL-Cell (Figure S2). The working electrode was prepared by carefully mixing the components (94.8 wt% $Li_2Ni_2W_2O_9$, 5 wt% Carbon Super P, 0.2 wt% PTFE) in ethanol, using an agate mortar and an agate pestle. The resulting powder was poured on a clean glass surface and repeatedly flattened with a glass cylinder until a ~0.5 mm film was obtained. This film was then dried at 80 °C in vacuum overnight.

The counter electrode was metallic lithium. The current collector on the working electode's side was an Al mesh, and one layer of Whatman GF/D glass fiber filter was used as a separator between the two electrodes. The electrolyte was a 1 M solution of lithium hexafluorophosphate ($LiPF_6$) in a 1:1:4 vol% mix of ethylene carbonate (EC), propylene carbonate (PC) and dimetyl carbonate (DMC). The cell was mounted on an inverted microscope (Axio Observer 7, Zeiss) and illuminated from the backside through a 63x oil immersion objective (Plan Apochromat, Zeiss, NA = 1.4) by means of an unpolarized white light source. A CMOS color camera (Axiocam 705 color, Zeiss) collected the reflected light through the same objective. Each image was taken manually, every 100 s, in order to maintain the focus on the working electrode through the experiment. The cell was cycled between 2.5 and 4.85 V vs Li^+/Li at a current density of 10 $mA.g^{-1}$, at room temperature, using a CHI 760E potentiostat from CH Instruments.

Transmission-like images (Figure S3) of pristine and delithiated LNWO particles were obtained by dispersing the electrode material (carbon + LNWO, see *Electrochemistry*) with a droplet of DMC on a glass coverslip, and by positioning a 25 µm-diameter Pt ultramicroelectrode (UME) above the particle, 10 µm above the glass surface, using an ElProScan scanning electrochemical probe microscope from HEKA. The Pt UME acts as a mirror reflecting the light transmitted by the particle towards the microscope objective.

The image analysis was carried out using homemade Python routines. For the statistical analysis, the images were first thresholded and then segmented into the different particles using the skimage.measure.label function from the scikit-image library[38]. From there, the average reflected intensity, I_{refl}, and the surface area in terms of pixels (pixel size = 55 nm), S, were extracted for each particle. The same method was used to extract I_{refl} over time for a given particle, in the single-particle-scale study. Lateral drift was corrected using the trackpy library[39]. Due to the nature of the data treatment, a few particle agglomerates were identified as “single particles”; this is especially true for the biggest agglomerates ($S > 10^5$ px).

Results

1 – Crystal structure

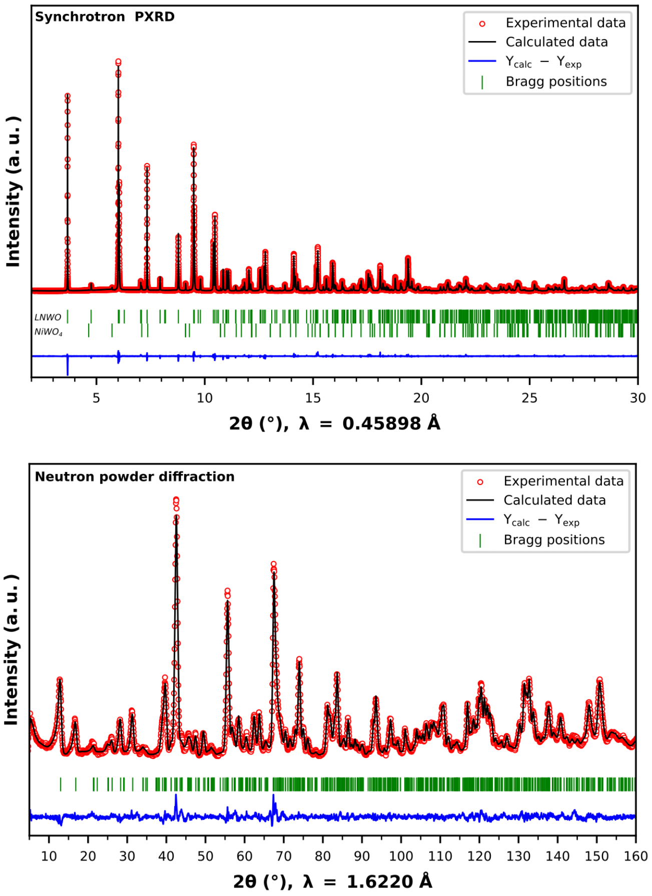

Figure 1 – Rietveld refinements of $Li_2Ni_2W_2O_9$ from the synchrotron XRD pattern (top) and neutron diffraction pattern (bottom) at room temperature (300 K). The red circles, black continuous line and bottom blue line represent the observed, calculated, and difference patterns respectively. Vertical green tick bars are the Bragg positions.

The crystal structure of $Li_2Ni_2W_2O_9$ was studied through X-ray and neutron powder diffraction. As little information was known about this new phase, the structure had to be solved *ab initio*. First, the X-ray diffraction peaks were indexed in an orthorhombic unit cell using the DICVOL program[40], with a volume of 632.29(2) Å^3 and lattice parameters a = 8.69523(8) Å, b = 5.06407(5) Å, and c = 14.34517(2) Å. The observed reflection conditions are consistent with the *Pbcn* space group. Thus, this space group was used to solve the structure of

$Li_2Ni_2W_2O_9$ using the FOX software[41]. The calculations were initialized assuming a structure built on NiO_6 octahedra. This led to an initial structural agreement with the X-ray powder diffraction pattern. Li atoms were placed in the structure using bond valence maps, which were calculated using the GFourier program from the FullProf Suite[42]. Their positions were confirmed through neutron powder diffraction. The final structural model was obtained through Rietveld refinements[34] simultaneously from the neutron and synchrotron X-ray powder diffraction patterns (Figure 1). Electron diffraction patterns (Figure S4) are in good agreement with the *Pbcn* space group and the lattice parameters determined from synchrotron powder XRD data.

Element	**Wyckoff site**	***x/a***	***y/b***	***z/c***	**B_{iso} (Å^2)**	**Occupancy**	**Bond valence sum[43]**
Li	8*d*	0.340(2)	0.522(4)	0.4947(6)	1.8(19)	1	0.944(2)
Ni	8*d*	0.6633(2)	0.5005(6)	0.81315(9)	0.364(17)	1	1.982(1)
W	8*d*	0.5242(4)	0.000(13)	0.6441(16)	0.022(4)	1	5.891(5)
O1	4*c*	1/2	0.281(11)	3/4	0.207(14)	1	1.989(2)
O2	8*d*	0.5083(4)	0.6791(7)	0.9091(2)	0.207(14)	1	1.933(3)
O3	8*d*	0.6494(4)	0.8518(7)	0.7469(2)	0.207(14)	1	1.945(2)
O4	8*d*	0.8426(5)	0.6635(6)	0.8952(19)	0.207(14)	1	1.831(2)
O5	8*d*	0.3386(5)	0.1539(6)	0.9257(19)	0.207(14)	1	2.114(3)

Space group: *Pbcn.* **Lattice parameters**: a = 8.69523(8) Å / b = 5.06407(5) Å / c = 14.34517(2) Å
V = 631.928(1) Å^3. Z = 4. **Reliability parameters**: χ^2 = 1.95, R_{Bragg} = 2.74 % (Synchrotron X-Ray) / χ^2 = 2.70, R_{Bragg} = 3.41 % (Neutron).

Table 1 – Results of the Rietveld refinements (Synchrotron PXRD and neutron powder diffraction) for *Pbcn* $Li_2Ni_2W_2O_9$. For oxygen atoms, B_{iso} values were all set equal.

The crystal structure of the $Li_2Ni_2W_2O_9$ phase is shown in Figure 2, and the main crystallographic parameters can be found in Table 1. The $Li_2Ni_2W_2O_9$ phase is nearly pure: two low-intensity peaks, at 2θ = 5.72° and 2θ = 9.11° on the synchrotron XRD pattern (Figure 1) indicate the existence of a small amount of *P*2/*c* $NiWO_4$ (ICSD n° 15852)[44] as an impurity (less than 2 wt%). The relative purity of the synthetized material and the homogeneous distribution of Ni and W were also confirmed through STEM-EDX compositional maps (Figure S5).

Based on Pauling's valence-sum rule[45], for a given ion, the sum of its bonds' valences should be equal to the ion's valence. Thus, thanks to calculation based on bond lengths[43], we find values suggesting that $Li_2Ni_2W_2O_9$ contains Li^+, Ni^{2+}, W^{6+} and O^{2-} (Table 1).

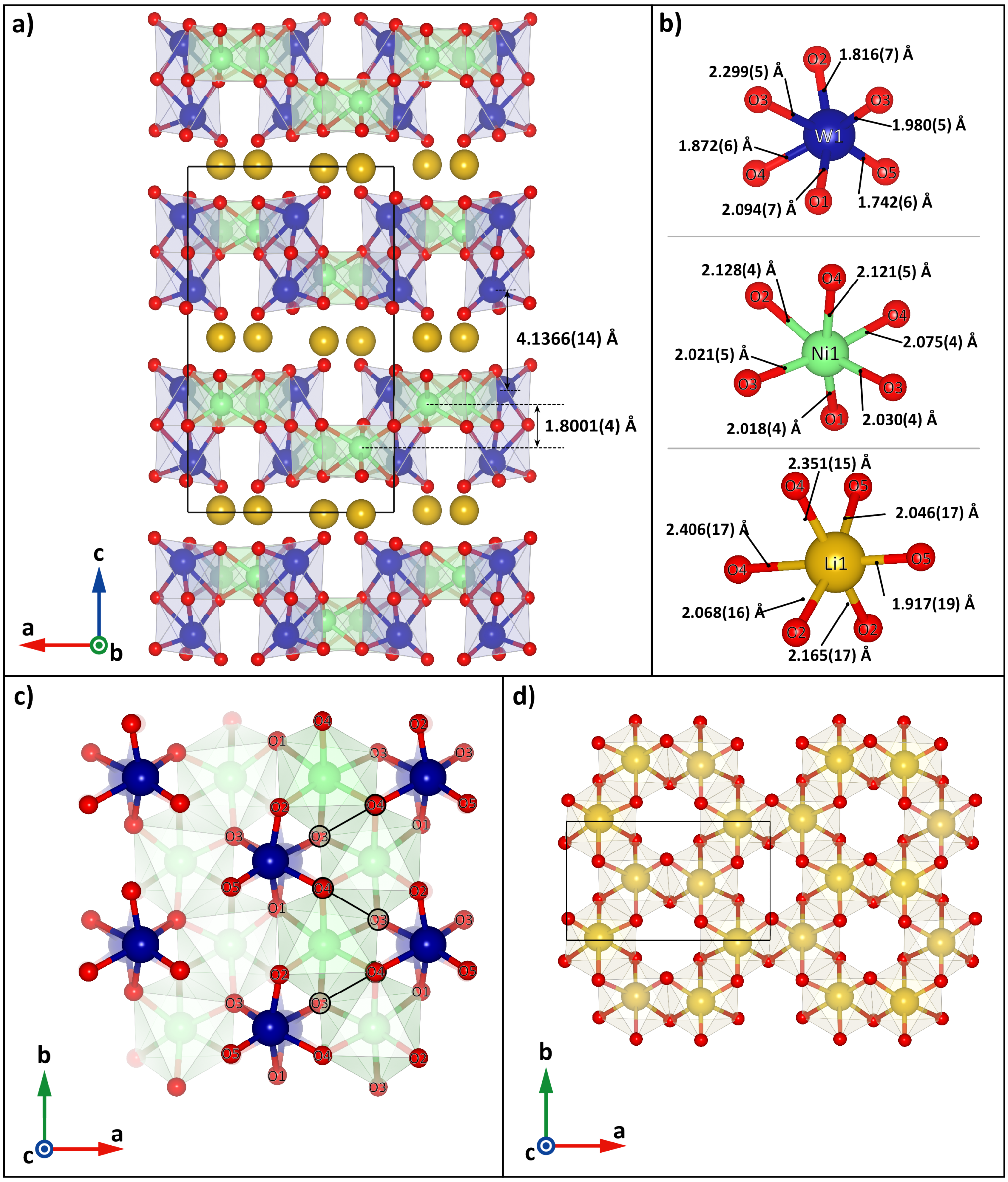

Figure 2 – Crystal structure of $Li_2Ni_2W_2O_9$. a) Projection along [010] of the layered structure. b) Bond lengths for the WO_6, NiO_6 and LiO_6 octahedra. c) Projection along [001] highlighting the NiO_6 chains in the Ni-W-O layers. Atoms in a paler color have lower z-coordinates. d) Projection along [001] highlighting the lithium honeycomb configuration in the interlayer. In these representations, tungsten atoms are blue, nickel atoms are green, lithium atoms are yellow, and oxygen atoms are red.

$Li_2Ni_2W_2O_9$ displays a layered structure (Figure 2a). The layers are composed of chains of edge-sharing NiO_6 octahedra; in a given layer, these chains alternate between a lower and an upper z-coordinate along the *c*-axis (Figure 2a,c). The chains are linked to each other by O1 oxygen atoms, and by face-sharing WO_6 dimers located between each chain as well. Each WO_6 octahedron shares three edges with a NiO_6 chain (O1-O4, O4-O3, O3-O2), a corner with another chain (O3) and a face with another WO_6 octahedron (O3-O3-O1) (Figure 2c).

Interestingly, the WO_6 octahedra are heavily distorted: the W-O bonds pointing toward the interlayer (W-O2, W-O4, W-O5) are much shorter than those pointing toward the Ni-W-O layer (W-O1, W-O3, W-O3) (Figure 2a,b,c). The opposite trend is observed when looking at the Ni-O bond lengths for the NiO_6 octahedra: the Ni-O bonds pointing toward the interlayer (Ni-O2, Ni-O4, Ni-O4) are longer than those pointing in the opposite direction (Ni-O1, Ni-O3, Ni-O3). However, the distortion is less significant for the NiO_6 octahedra than for the WO_6 octahedra. The distortion for an octahedron can be quantified by looking at its quadratic elongation[46], given by equation (I):

$$\langle\lambda\rangle = \frac{1}{6}\sum_{i=1}^{6}\left(\frac{l_i}{l_0}\right)^2 \tag{I}$$

where l_0 is the vertex-to-center distance for a regular octahedron of equal volume to the distorted polyhedron, with bond lengths l_i. For $\langle\lambda\rangle = 1$, the studied octahedron displays no distorsion. The quadratic elongation for a WO_6 octahedron in the $Li_2Ni_2W_2O_9$ phase is 1.06, whereas it is merely equal to 1.02 for a NiO_6 octahedron. These values highlight the severity of both the bond angles and bond lengths distortions in the WO_6 octahedra compared to the NiO_6 octahedra. Such distortions may arise from a second order Jahn-Teller effect, which is rather common for high-valence d^0 cations[47,48].

The most interesting feature of the crystal structure of $Li_2Ni_2W_2O_9$ comes from the lithium ions, which occupy the interlayer space, forming a "honeycomb" pattern (Figure 2d). Each lithium ion is located directly above/below a nickel ion, with a distorted octahedral coordination. Here, the longest Li-O bonds, Li-O4, point toward the neighboring NiO_6 octahedron, in such a way that the Li^+ cations are always closer to one Ni-W-O layer than the other. In particular, the Li^+ ions are always closer to the W^{6+} ions than the Ni^{2+} ions (Figure 2a,b,d). This could be explained by the high valency of the W^{6+} ions, which have to get closer to low-valence cations (Li^+) to maintain local charge neutrality; this would also justify why the W^{6+} cations seem to deviate from the Ni^{2+} cations (Figure 2c)[47,48].

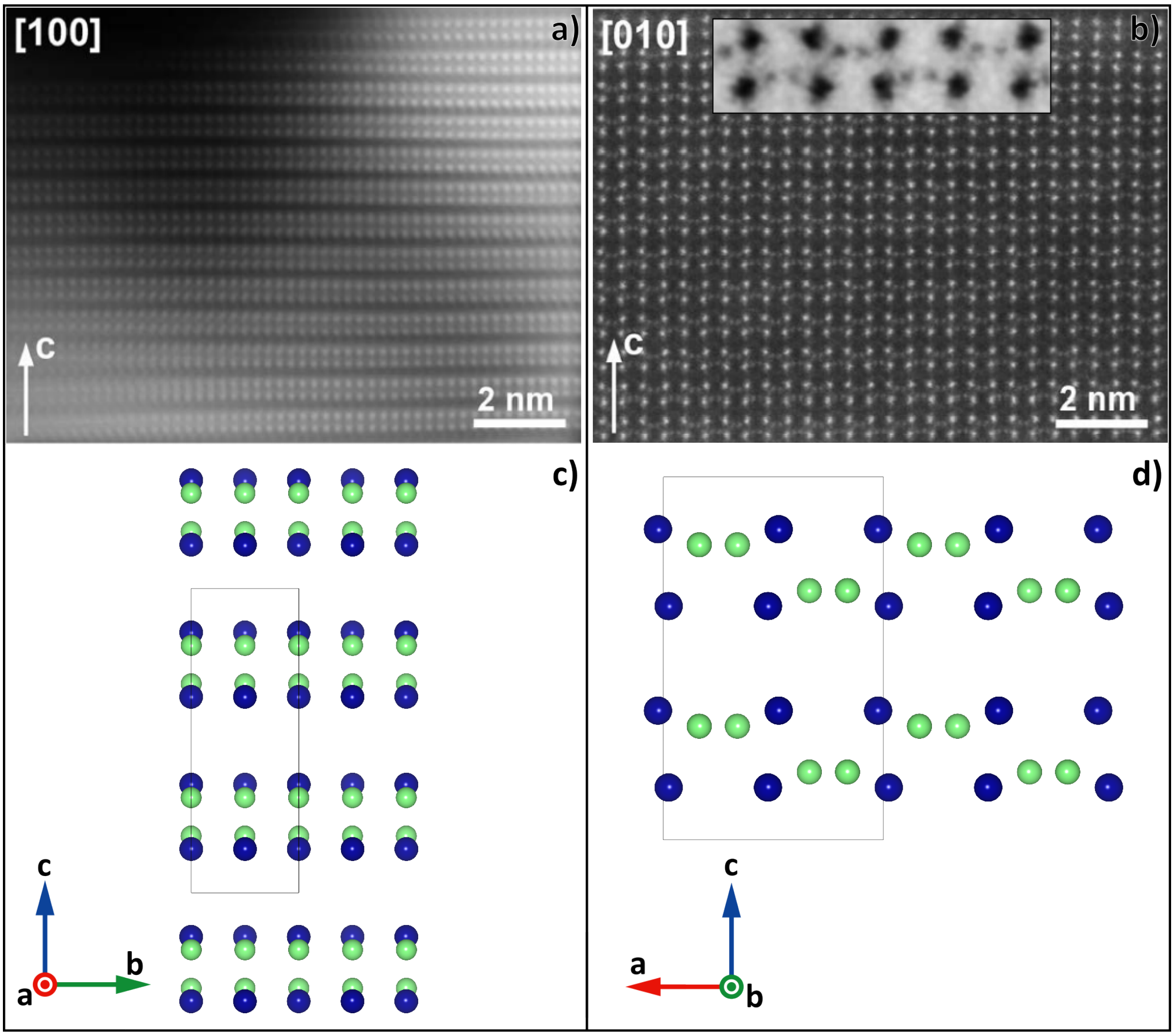

Figure 3 – HAADF-STEM images along a) the [100] direction and b) the [010] direction for a $Li_2Ni_2W_2O_9$ crystallite. The inlet in b) comes from the same HAADF-STEM image, in inverted contrast and zoomed in to highlight the positions of the Ni cations. c, d): Projections of the nickel and tungsten atoms position for the refined *Pbcn* $Li_2Ni_2W_2O_9$ structural model, along the c) [100] direction and d) [010] direction.

In order to validate the solved structure, $Li_2Ni_2W_2O_9$ was further analyzed by atomic resolution HAADF-STEM imaging (Figure 3a,b). On these images, the brightest dots represent the tungsten atoms, which possess the highest atomic number; nickel atoms can be seen as slightly dimmer dots in Figure 3b. Lithium cannot be detected due to its very small atomic number. In Figure 3a, we can observe rows of bright dots which are two-dot wide, and correspond to atomic columns consisting of both nickel and tungsten atoms. These rows of dots are separated by a dark space corresponding to the interlayer gap described before. This placement of the tungsten and nickel atoms fully matches with the structure we obtained through Rietveld refinement (Figure 3c). In Figure 3b, two-atom wide rows of bright dots (W) are observed when the structure is viewed along the [010] direction. A pair of dim dots (Ni) can be seen between the bright dots of each row; the position of each of these “dim pairs” alternates between the top and the bottom of the row. This configuration for the Ni and W atoms also matches quite well with the configuration found in the refined crystal structure (Figure 3d). Moreover, the W-W distance along the *c*-axis can be estimated to roughly 4 Å from the HAADF-STEM images, in agreement with the distance calculated from the structural model.

Many insertion materials studied for an application as cathode in lithium-ion batteries display a layered structure: $LiCoO_2$[49,50], NMC materials ($Li[Ni_xCo_{1-2x}Mn_x]O_2$)[51,52], $LiFeSO_4OH$[53], and $Li_4VO(PO_4)_2$[54], to name a few. However, although it is also a layered compound, $Li_2Ni_2W_2O_9$ has a structure that is quite unique compared to what can be found among other cathode materials, namely because of its resemblance with corundum. As such, its electrochemical properties as a potential electrode material for Li-ion batteries were studied.

2 – Electrochemical behavior

80 wt% $Li_2Ni_2W_2O_9$ powder (LNWO) was mixed with 20 wt% carbon black to prepare the cathode electrode, which was then cycled against lithium metal through a galvanostatic charge-discharge process. The resulting curves are shown in Figure 4.

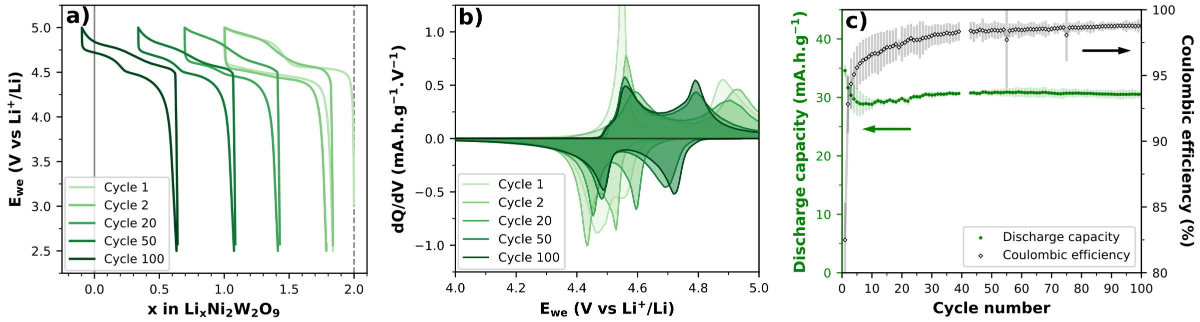

Figure 4 – a) Galvanostatic charge-discharge curves and b) dQ/dV curves for LNWO + 20 wt% carbon black, cycled at 10 mA.g^{-1} against Li metal at room temperature; the electrolyte was a solution containing 1 M $LiPF_6$ in a 1:1:4 EC:PC:DMC mix. c) Average discharge capacity (green dots) and average coulombic efficiency (black diamonds) for three coin cells cycled according to the conditions set in a).

When cycled between 2.5 and 5.0 V vs Li^+/Li at a current density of 10 mA.g^{-1}, LNWO displays two distinct plateaus in its first charge: one appears at around 4.55 V vs Li^+/Li with a capacity of 23 mA.h.g^{-1}, while the other one appears above 4.8 V vs Li^+/Li, contributing a capacity of 18 mA.h.g^{-1} (Figure 4a). In the following discharge, two slopes can be observed, but in a much narrower potential region: the first slope appears between 4.6 and 4.5 V vs Li^+/Li, and the other between 4.5 and 4.4 V vs Li^+/Li. This behavior indicates that we have two distinct redox couples. This electrochemical activity is certainly due to the nickel cations: Ni^{2+} is the only cation that can be oxidized in the pristine compound. This was confirmed by XAS measurements (Figure S7). However, the potentials at which the reactions occur are significantly higher than for other layered, nickel-active battery materials: an oxidation potential ranging from 3.8 to 4.3 V vs Li^+/Li is expected for the Ni^{3+}/Ni^{2+} redox couple[51,52,55,56]. The increase in the active potential range of $Li_2Ni_2W_2O_9$ may be explained by an inductive effect between the Ni^{2+} cations and the WO_6 octahedra, similarly to what can be found in $LiNiPO_4$[57–59].

Looking at the dQ/dV curves (Figure 4b), the first redox couple is initially characterized by a 100-mV polarization; this value increases slightly in the early cycles due to a shift of the reduction peak to lower potentials. However, this peak goes back to its initial position after cycle 50, and a 100-mV polarization is observed again. For the second, high-potential redox couple, the polarization decrease is much more significant: between cycle 2 and cycle 50, it goes from more than 400 mV to around 80 mV. This indicates that there is a kinetic limitation to the second redox couple, which decreases through an activation process after several cycles. Because the oxidation potential diminishes steadily, the charge associated with the second oxidation plateau increases: at cycle 50, the plateau fully appears in the charge profile. Overall, the activation process of LNWO leads to variations in discharge capacity: it decreases to from 34 to 29 $mA.h.g^{-1}$ between cycles 1 and 7 before steadily increasing back to 31 $mA.h.g^{-1}$ in the subsequent cycles (Figure 4c). After 100 cycles, the material displays a capacity retention of 84 % when compared to the 1st cycle; this value increases to 98 % if cycle 50 is taken as the reference point. Although this activation process is reminiscent of what has been reported on electrochemical grinding in other materials[60], the capacity increase is actually quite small, and SEM pictures taken before and after cycling (Figure S8) show no clear evolution of the material's morphology correlated to the polarization decrease.

An irreversible capacity of ~7 $mA.h.g^{-1}$ is observed in the first cycle. This irreversibility between charge and discharge tends to decrease through the cycles, as indicated by a decrease in the slippage of the cycling curves, and by a steady increase in coulombic efficiency; however, this efficiency remains below 99 %, indicating that some irreversible processes are still occurring during charges. Such irreversibility could be associated with electrolyte decomposition, which would not be surprising considering how carbonate-based electrolytes suffer from high-potential cycling[61].

In order to get a better picture of the electrochemical mechanism involved in LNWO, an *operando* XRD experiment was performed, using the same cycling conditions as before. The results of this experiment are shown in Figure 5.

Upon removing lithium from LNWO, we observe that the (00*l*) peaks shift toward lower Bragg angles (Figure 5b), while (*hk*0) peaks shift toward higher Bragg angles (Figure 5a), which matches with an increase in the *c*-lattice parameter, and a decrease in the *a*- and *b*-lattice parameters, respectively. The lattice expansion along the *c*-axis is easily explained by an increase of the coulombic repulsion between Ni-W-O layers upon Li^+ removal. Meanwhile, the oxidation of Ni^{2+} leads to a shortening of the Ni-O bond lengths, responsible for the lattice contraction along the *a*- and *b*-axis.

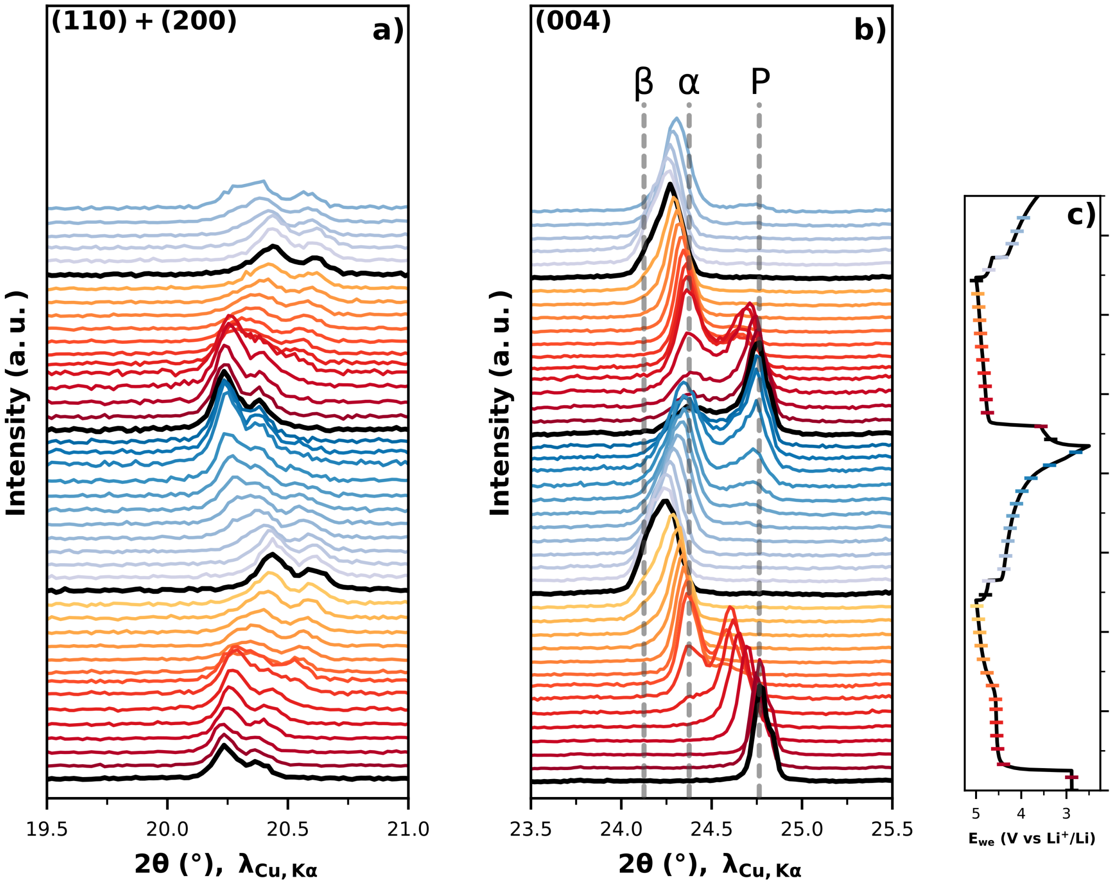

Figure 5 – Focus on the a) (110) + (200) peaks and b) (004) peaks of an *operando* XRD experiment on $Li_2Ni_2W_2O_9$. The scans taken during charge are in red; those taken during discharge are in blue. P: peak for $Li_2Ni_2W_2O_9$. α: peak for $Li_\alpha Ni_2W_2O_9$. β: peak for $Li_\beta Ni_2W_2O_9$. c) Cycling curve (E_{we} against time, 10 mA.g^{-1}, 20 wt% carbon black) for the *operando* XRD experiment.

Moreover, after removing roughly 0.27 Li^+ equivalents from the material, new peaks start to appear indicating a biphasic system, matching with the first redox plateau. This underlithiated phase crystallizes in the *Pbcn* space group, similarly to the pristine phase; however, the underlithiated lattice is elongated along the *c*-axis (Table 2). As the peaks for the pristine phase have fully disappeared after removing 0.5 to 0.6 Li^+, the chemical formula for the underlithiated phase can be written as $Li_\alpha Ni_2W_2O_9$, with α between 1.4 and 1.5.

When more lithium is removed (up to 1.04 Li^+), the peaks of $Li_\alpha Ni_2W_2O_9$ keep shifting, and new shoulder peaks start to appear at positions matching with the (002) and (004) reflections. These could correspond to another biphasic and an even more underlithiated phase, $Li_\beta Ni_2W_2O_9$, with $\beta < \alpha < 2$. However, these shoulder peaks are not as defined as for the previous biphasic. Thus, the existence of this second biphasic is not as clear-cut, even though those two biphasic systems would match pretty neatly with the two sets of plateaus/peaks observed in Figure 4a,b.

	a **(Å)**	***b*** **(Å)**	***c*** **(Å)**	**V (Å^3)**
$Li_2Ni_2W_2O_9$	8.69523(8)	5.06407(5)	14.34517(2)	631.928(1)
$Li_\alpha Ni_2W_2O_9$	8.630(12)	5.0534(6)	14.605(17)	637.0(14)

Table 2 – Lattice parameters calculated through Rietveld refinements of the pristine $Li_2Ni_2W_2O_9$ XRD pattern (Synchrotron PXRD), and of the underlithiated $Li_\alpha Ni_2W_2O_9$

An opposite trend in the evolution of the XRD patterns is observed when reinserting lithium, indicating that the structural changes occurring in the LNWO electrode are reversible. This reversibility is only partial, however, as the peaks associated to $Li_\alpha Ni_2W_2O_9$ do not fully disappear at the end of the discharge. This slight structural irreversibility accounts for the 0.2 Li^+ that cannot be inserted back in the material during the first discharge and is responsible for the 7 mA.h.g^{-1} irreversibility in the first cycle. In general, the structure of the material does not appear to deteriorate significantly past the first cycle (Figure S8); this could explain the good reversibility and capacity retention observed for LNWO, and it would indicate that structural irreversibilities do not contribute much further to the electrochemical irreversibility past the first couple of cycles..

A similar set of electrochemical characterizations was conducted on $Li_2Ni_2W_2O_9$ with a lower potential range (1.0 to 3.0 V) to inspect the electrochemical behavior of the phase upon overlithiation. The results suggest that an irreversible conversion reaction occurs when cycling LNWO in this potential window (Figures S9, S10), and $Li_2Ni_2W_2O_9$ is probably transformed into an amorphous mix of different phases after the first discharge to 1.0 V, which is not unheard of for a nickel-tungsten mixed oxide[62].

3 – Optical properties

Our *operando* XRD measurements demonstrate that the reversible electrochemical behavior of $Li_2Ni_2W_2O_9$ at high potentials is also associated to reversible structural changes. Considering this, one might wonder if reversible optical changes are not occurring as lithium is inserted or removed from the material.

In order to assess the electrochromic properties of $Li_2Ni_2W_2O_9$, we performed an *operando* optical reflection microscopy experiment. As schematized in Figure 6a, the images recorded correspond to collection of light reflected by the imaged sample. A self-standing electrode (LNWO: 94.8 wt% / Carbon black Super P: 5 wt% / PTFE: 0.2 wt%) was cycled against lithium metal in a cell designed for this type of experiment (see Figure S2)[24,25]. The full setup for the experiment is shown in Figure 6a.

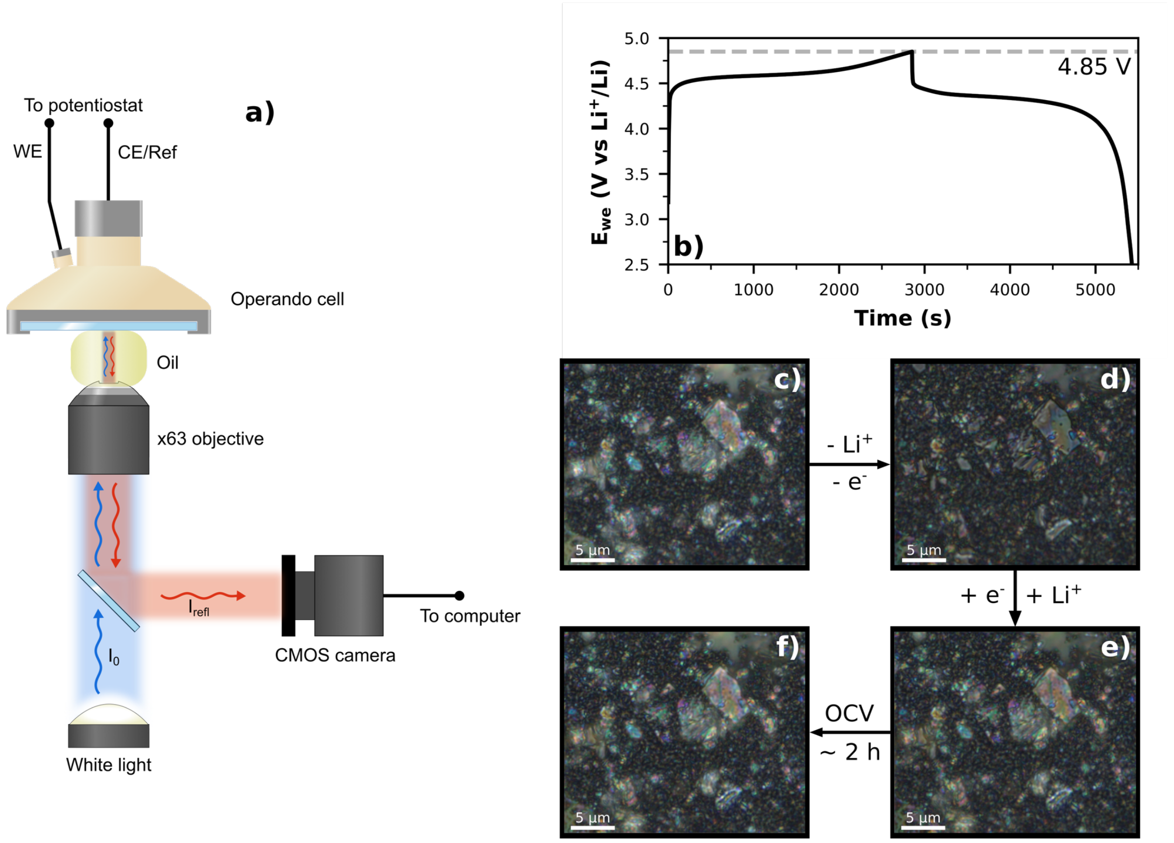

Figure 6 – a) *Operando* optical reflection microscopy setup. b) Galvanostatic charge-discharge curve (E_{we} vs time) for the working electrode during the operando optical microscopy experiment. c), d), e), f): Optical microscopy pictures taken before the experiment, at the end of the charge, at the end of the discharge, and 2 h hours after the end of the experiment, respectively.

The cell was cycled from 2.5 V to 4.85 V vs Li^+/Li (Figure 6b), granting an insight on what was occuring optically to LNWO during Li^+ (de)insertion, but only for the first redox plateau. The optical microscopy images collected by the CMOS camera (Figure 6c, d, e, f) clearly show a general decrease of the reflected intensity (I_{refl}) for the LNWO particles after the removal of lithium cations; the reflected intensity increases back after the reinsertion of Li^+. Moreover, from transmission-like images of pristine and delithiated LNWO particles aquired *ex situ* (*in situ* experiments in tranmission mode are impossible due to the electrode's thickness), we see that the transmitted intensity is also attenuated upon Li^+ deinsertion (Figure S3). Since both reflectance and transmittance decrease during Li^+ deinsertion, this necessarily means that the absorbance of light by the particles increases.Therefore, it is confirmed that $Li_2Ni_2W_2O_9$ is an anodic electrochromic material.

The reflection microscopy data was further treated in order to quantify the intensity reflected by each LNWO particle throughout the experiment and to perform a statistical analysis (Figure 7).

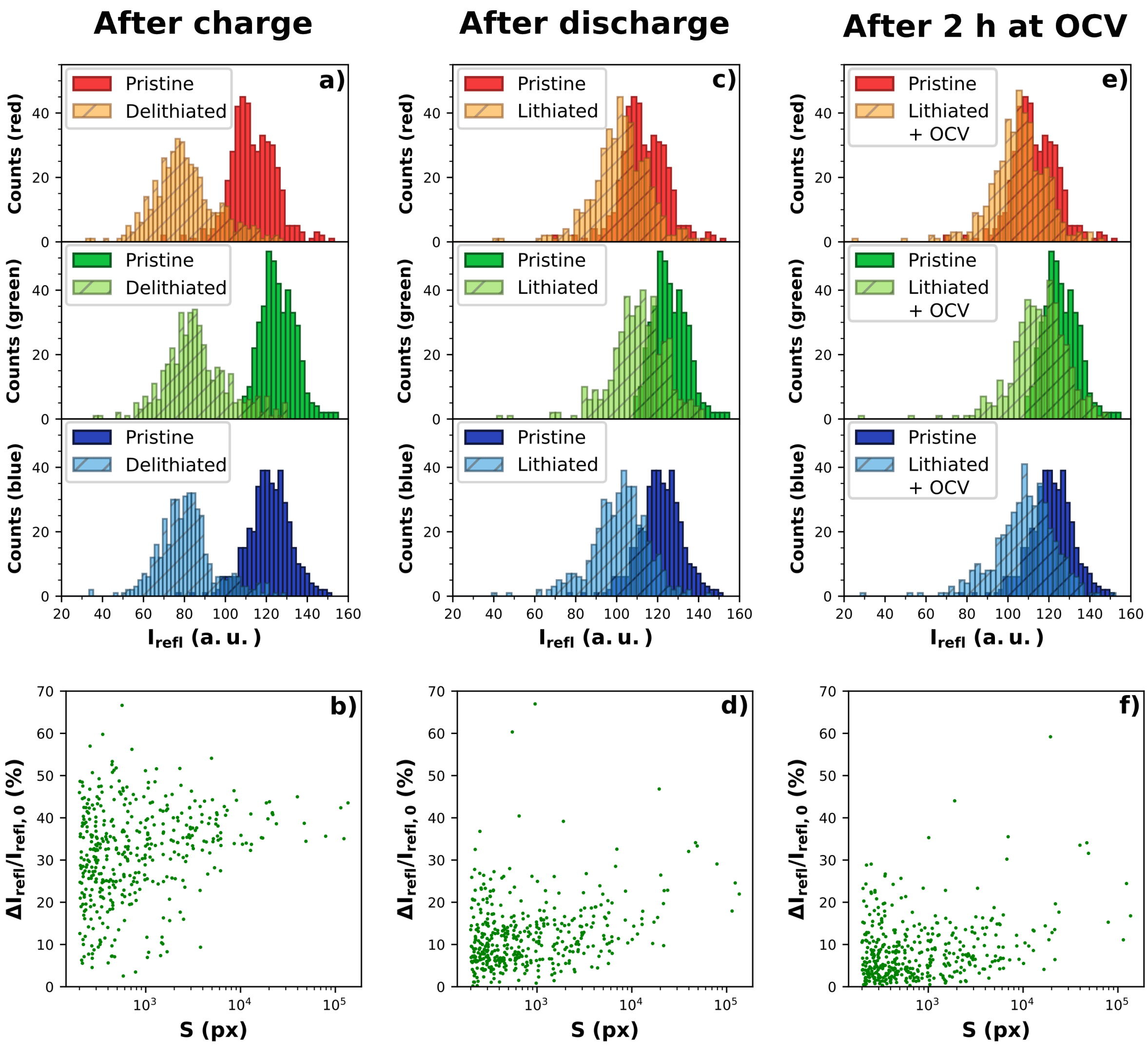

Figure 7 – Top: distributions of the intensity reflected by each particle of the optical microscopy picture on the three RGB channels. Bottom: relative variation of the reflected green intensity ($I_{refl}/I_{refl,0} - 1$) against particle surface S (S is given as the number of pixels required to represent each particle; pixel size = 55 nm). The pristine particles were taken as reference ($I_{refl,0}$). a), b): Pristine vs delithiated particles. c), d): Pristine vs lithiated particles. e), f): Pristine vs lithiated particles after 2 hours at OCV.

The global trend observed in Figure 6 is confirmed: across all three RGB channels, there is a decrease of reflected intensity after the delithiation and an increase after the lithiation. Interestingly, we can also observe that there is a slight increase of the reflected intensity when leaving the electrode at OCV for two hours after the lithiation, compared to what is seen immediately at the end of the discharge (Figure 7c,e). This suggests that the lithium insertion inside the material iskinetically limited, possibly by the contraction of the crystal lattice along the *c*-axis during discharge[63]. Despite this slight increase after the resting time, the electrode does not fully go back to its original optical state: on all RGB channels, the intensity reflected by the electrode is slightly lower after the experiment compared to the pristine material (Table

3). This optical irreversibility matches with the electrochemical (Figure 4) and structural irreversibilities (Figure 5) displayed by the material when cycled against lithium.

Channel	Pristine	Delithiated	Lithiated	Lithiated + OCV
Red	μ = 113 σ = 11	μ = 80 σ = 16	μ = 101 σ = 16	μ = 104 σ = 17
Green	μ = 126 σ = 8	μ = 85 σ = 16	μ = 110 σ = 16	μ = 114 σ = 18
Blue	μ = 121 σ = 10	μ = 81 σ = 14	μ = 100 σ = 16	μ = 107 σ = 18

Table 3 – Results for the gaussian fits of distributions of intensities reflected by each particle, on the three RGB channels, during the first charge-discharge cycle of the operando microscopy experiment. μ: expected value. σ: variance. Number of particles (sample size): 425.

It is also interesting to see that optically-wise, not all particles in the electrode behave in the same way. This is especially noticeable when looking at Figure 7b : the relative intensity decrease between the particles in their pristine and delithiated states can range from 5.6 % to 67 %, depending on the particle studied and, to some extent, its size. This highlights the importance of looking at what is occuring over time at the single-particle-level, in order to complete the information acquired from the global picture.

Looking at the evolution of the average reflected intensity at the single-particle-level over time throughout the charge-discharge process (Figures 8, 9, S11), the same general trends are observed: a decrease in intensity upon delithiation, an increase upon lithiation. However, some particles can be fully darkened in less than 1000 s (particle *a*, particle *c*), while others require close to the entire charging time to go through the same optical transition (particle *b*). More examples can be found in Figure S12. This indicates that no clear correlation exists between the electrochromic kinetics and the particle size during the charge (Figure S13), possibly due to the somewhat heterogeneous properties of the LNWO particles (density, thickness, defects, etc.).

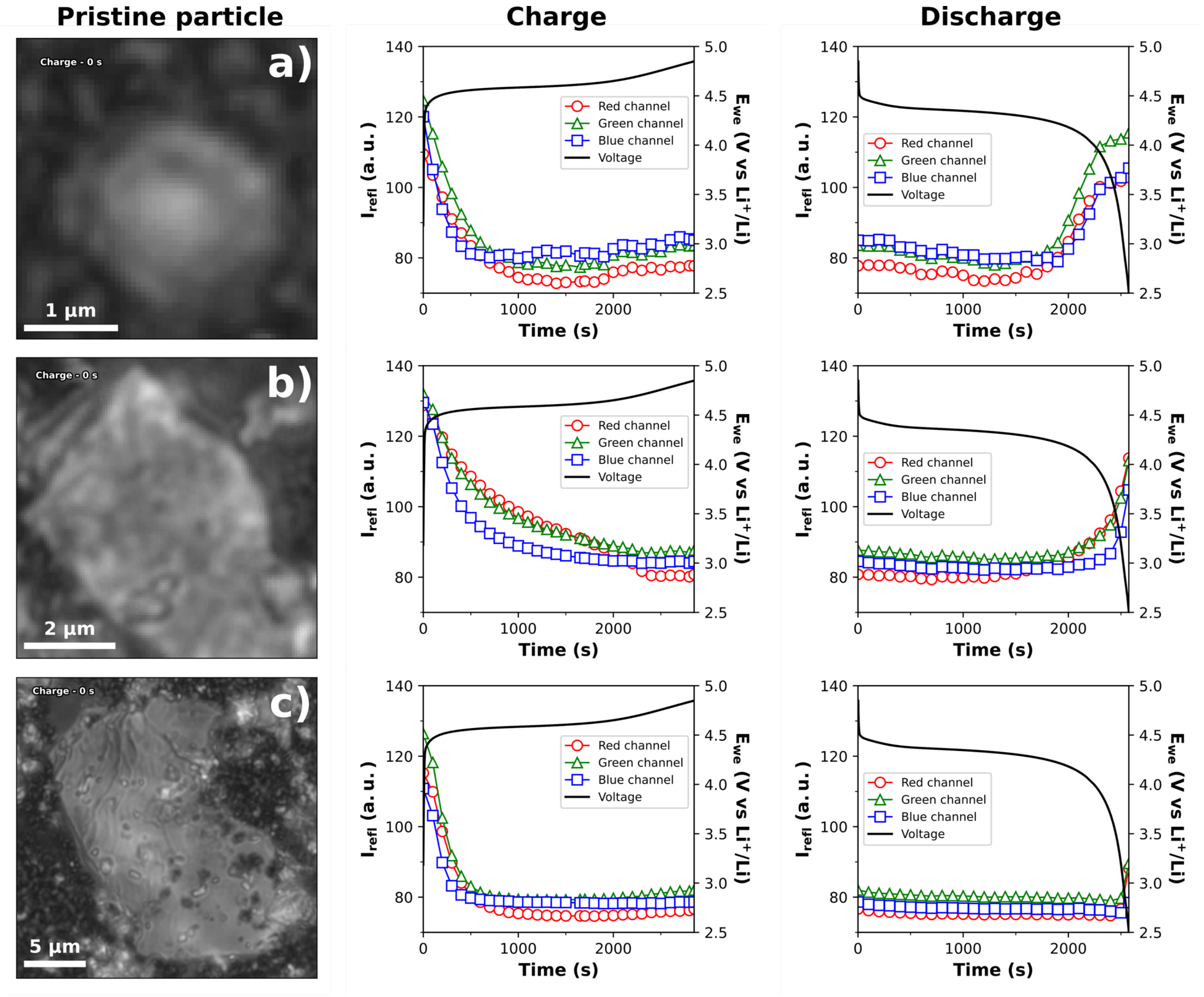

Figure 8 – Optical behavior during the galvanostatic charge-discharge for different particles (a, b, c). From left to right: gray-scaled optical microscopy picture in the electrode's pristine state, I_{refl} and E_{we} vs time during the charge, and I_{refl} and E_{we} vs time during the discharge.

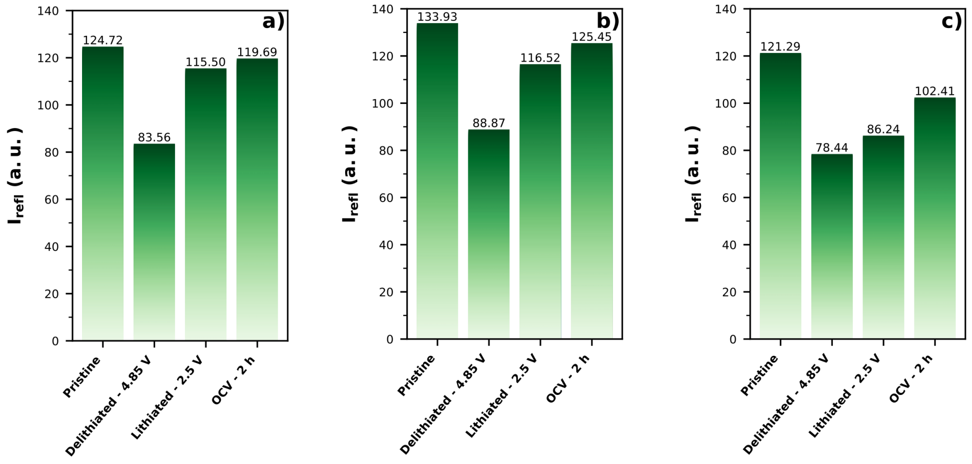

Figure 9 – Evolution of the reflected intensity on the green channel for particles a, b and c shown in Figure 8. I_{refl} is given for the pristine particles, the particles after charge, the particles after discharge and the particles two hours after the discharge.

The similarity between the slopes of the I_{refl} curves in charge and discharge suggest that Li^+ cations are inserted, during the discharge, (at least initially) at the same rate as they are deinserted during the charge. Besides, the reversibility of the optical evolution during charge and discharge is highly dependent on the particle size. For smaller particles, such as particle *a*, the optical variation is nearly symmetrial between charge and discharge (Figure 8a), with slow lithium-insertion kinetics by the end of the discharge leading to some irreversibility in the reflected intensity (Figure 9a). However, upon increasing the particle size (particle *b* and *c*), the shapes of the curves for I_{refl} = f(t) differ severely between the charge and the discharge. More specifically, the recovery of the reflected intensity during discharge happens less and less, and later and later from particle *a* to *c* (Figure S14), and as such, the optical irreversiblities become larger (Figures 8, 9); for particle *c*, the reflected intensity only increases a bit at the very end of discharge (Figure 8c). This can be explained by the poorer Li^+ insertion kinetics of the larger particles during lithiation, which also affects the electrochromic kinetics during discharge as both are related to each other. Worth mentioning is that such limitations of the Li^+ insertion kinetics, which mostly happen during discharge, are actually very common for the layered Ni-containing Li-ion cathode materials[64–66].

This optical study at the single-particle-level grants us more information on the source of the irreversibility which can be observed on cycling curves for cells using $Li_2Ni_2W_2O_9$ as a working electrode (Figure 4a). During the first cycle, and especially the first discharge, the insertion of Li^+ cations inside the material is kinetically limited, possibly because of a structural contraction of the particles at the edges. As such, reversible lithium insertion inside the biggest particles is not favored, meaning that these particle become at least partially inactive. Meanwhile, for smaller, submicrometric particles, the slow rate of lithium insertion keeps them from going back to their initial, fully lithiated state.

The fact that variations in I_{refl} do not occur immediately after the beginning of the discharge can be explained by a simple top-to-bottom conversion model of the particles (Figure S15). Based on this model, a threshold amount of Li^+ needs to be inserted inside a particle before I_{refl} starts increasing, because changes in I_{refl} can only be observed once a threshold thickness of lithiated phase (< 200 nm) remains in the particle.

Going to higher voltage (above 4.9 V vs Li^+/Li) induces detrimental parasitic reactions in the cell, and therefore, the optical changes related to the second redox plateaus were not studied. However, most optical changes seem to occur during the first plateau and specifically in the early stages of this first plateau.

Discussion

The crystal structure of $Li_2Ni_2W_2O_9$ derives from the corundum structure, with a pseudo-hexagonal lattice. Materials with similar lattice structures can frequently be found in the litterature, the most prominent being the aforementioned corundum, also known as α-Al_2O_3[67]. In fact, it is very easy to transform the lattice of α-Al_2O_3 ($R\overline{3}c$) into the orthorhombic, *Pbcn* lattice ($Li_2Ni_2W_2O_9$) through the following set of equations:

$$\begin{cases} a_{Pbcn} = a_{R\bar{3}c} - b_{R\bar{3}c} \\ b_{Pbcn} = a_{R\bar{3}c} + b_{R\bar{3}c} \\ c_{Pbcn} = c_{R\bar{3}c} \end{cases} \qquad \text{(II, III, IV)}$$

Compared to α-Al_2O_3, however, $Li_2Ni_2W_2O_9$ is a compositionally mixed oxide. There are many examples of binary or ternary oxides displaying a corundum-like structure ($Co_4Nb_2O_9$[68], Ni_3TeO_6[69], Mn_2ScTaO_6[70], $Li_2Mg_2W_2O_9$[71], Li_2GeTeO_6[72], etc.). In fact, the crystal structure of $Li_2Ni_2W_2O_9$ matches with that of another compound, $MgNi_3Nb_2O_9$[73], which displays (Mg,Ni)-honeycomb layers caught between Mg-Ni-Nb-O layers made of octahedra chains, in a pattern similar to what can be seen in $Li_2Ni_2W_2O_9$ (Figure 2). A few reports have been made on materials with a $MgNi_3Nb_2O_9$-type structure[74,75] (also known as “ramsayite” structure); however, as far as we know, none of them display lithium layers.

Thus, what truly sets $Li_2Ni_2W_2O_9$ apart from other corundum-like materials is a combination of characteristics: an ordered structure, an interlayer suitable for lithium diffusion and an electrochemically active 3d transition metal.

This opens a wide array of possibilities for the synthesis of new materials to use as cathodes for the electrochemical (de)insertion of lithium. For instance, replacing the divalent nickel in $Li_2Ni_2W_2O_9$ with another divalent transition metal, or tungsten with another, lighter element, would make for interesting synthesis prospects. As it is a ternary oxide, it might be possible to tune the electrochemical and optical properties of the material by changing one or more elements in the composition.

Indeed, as it stands, LNWO displays a reversible specific capacity of roughly 31 $mA.h.g^{-1}$ past its initial capacity fade, which is much too low to compete with other Li-ion battery cathode materials. This low specific capacity stems mainly from its very high molar mass (642.89 $g.mol^{-1}$). $LiFePO_4$[76] and $LiNi_{1/3}Mn_{1/3}Co_{1/3}O_2$[77] typically display specific capacities between 160 and 175 mA.h.g^{-1} when cycled in their standard potential windows. Trying to find materials with a similar structure to LNWO, but with lighter constituting elements, could be a path to the discovery of new cathode materials for energy storage.

On top of this, playing with the nature of the transition metals could open the door to a new family of electrochromic materials (Figure S16). However, a proper assessment of the electrochromic performances of $Li_2Ni_2W_2O_9$ still needs to be done. In order to do this, the compound must be prepared as a thin film, and an in-depth study of its optical properties will be required.

Conclusion

A new material, with chemical formula $Li_2Ni_2W_2O_9$, was synthetized through solid-state synthesis. It crystallizes in the orthorhombic *Pbcn* space group; its layered structure was identified through synchrotron XRD, neutron diffraction and TEM. $Li_2Ni_2W_2O_9$ is, as far as we know, the first electrochemically active compound with an ordered, corundum-like structure and lithium "honeycomb" layers. The cycling capabilities of this new material against Li metal were assessed: it displays two active redox systems, with a low reversible capacity of roughly 31 mA.h.g^{-1}, good reversibility and good capacity retention over 100 cycles. Through an *operando* optical microscopy experiment, it was established that this material displays anodic electrochromism, thanks to the Ni^{3+}/Ni^{2+} redox couple which is active upon (de)lithiation. On top of granting information about the eletrochromic properties of $Li_2Ni_2W_2O_9$, this optical microscopy experiment delivered some insights into the source of the electrochemical and structural irreversibilities displayed by the material: the lithiation of the particles is kinetically limited, and bigger particles become partially inactive after the first cycle.

Supporting Information

Experimental setups for *operando* XRD, *operando* reflection optical microscopy and *post-mortem* "transmission-like" microscopy. Electron diffraction patterns for $Li_2Ni_2W_2O_9$ powder. HAADF-STEM and EDX images for $Li_2Ni_2W_2O_9$ powder. SEM pictures of $Li_2Ni_2W_2O_9$ powder and self-standing electrodes. XAS study of $Li_2Ni_2W_2O_9$ in different states of charge. Study of the impact of long cycling of $Li_2Ni_2W_2O_9$ by XRD and SEM. Cycling behavior of $Li_2Ni_2W_2O_9$ at low potentials (3.0 – 1.0 V vs Li^+/Li). Study of the electrochemical behavior of $Li_2Ni_2W_2O_9$ at 1.5 mA.g^{-1}. Further examples of single particles studied through *operando* reflection optical microscopy. t_0 mapping of the *operando* reflection optical microscopy images. Top-to-bottom conversion model for the $Li_2Ni_2W_2O_9$ particles. Optical behavior of $Li_2Ni_2W_2O_9$ over three charge-discharge cycles. Sequential imaging for $Li_2Ni_2W_2O_9$ single particles (Figure S1 to S18, Table S1).

CIF file for $Li_2Ni_2W_2O_9$ powder.

Acknoledgements

The authors thank M. Avdeev for performing neutron powder diffraction experiments at the Echidna diffractometer at the OPAL reactor of ANSTO, R. Pandya for helping with the *operando* optical microscopy cell, and A. Iadecola for carrying out the XAS measurements at the ROCK beamline of the SOLEIL synchrotron. A. M. Abakumov thanks the Advanced Imaging Core Facility (AICF) of Skoltech for providing access to TEM. Use of the Advanced Photon Source at Argonne National Laboratory was supported by the U. S. Department of Energy, Office of Science, Office of Basic Energy Sciences, under Contract No. DE-AC02-06CH11357. S. Redor thanks the Association Nationale de la Recherche et de la Technologie (ANRT, France) for funding his Ph.D. project (ANRT-CIFRE n° 2021-0960).

Bibliography

(1) Platt, J. R. Electrochromism, a Possible Change of Color Producible in Dyes by an Electric Field. *J. Chem. Phys.* **1961**, *34* (3), 862–863. https://doi.org/10.1063/1.1731686.

(2) Deb, S. K. A Novel Electrophotographic System. *Appl. Opt.* **1969**, *8* (S1), 192. https://doi.org/10.1364/AO.8.S1.000192.

(3) Granqvist, C. G. Oxide Electrochromics: Why, How, and Whither. *Sol. Energy Mater. Sol. Cells* **2008**, *92* (2), 203–208. https://doi.org/10.1016/j.solmat.2006.10.027.

(4) Yang, P.; Sun, P.; Mai, W. Electrochromic Energy Storage Devices. *Mater. Today* **2016**, *19* (7), 394–402. https://doi.org/10.1016/j.mattod.2015.11.007.

(5) Cannavale, A.; Ayr, U.; Fiorito, F.; Martellotta, F. Smart Electrochromic Windows to Enhance Building Energy Efficiency and Visual Comfort. *Energies* **2020**, *13* (6), 1449. https://doi.org/10.3390/en13061449.

(6) Abergel, T.; Dean, B.; Dulac, J.; Hamilton, I.; Wheeler, T. *Global Status Report - Towards a Zero-Emission, Efficient and Resilient Buildings and Construction Sector*; 2018. https://wedocs.unep.org/bitstream/handle/20.500.11822/27140/Global_Status_2018.pdf?sequence=1&isAllowed=y (accessed 2022-05-13).

(7) Granqvist, C. G. Electrochromics for Smart Windows: Oxide-Based Thin Films and Devices. *Thin Solid Films* **2014**, *564*, 1–38. https://doi.org/10.1016/j.tsf.2014.02.002.

(8) Atak, G.; Bayrak Pehlivan, İ.; Montero, J.; Granqvist, C. G.; Niklasson, G. A. Electrochromic Tungsten Oxide Films Prepared by Sputtering: Optimizing Cycling Durability by Judicious Choice of Deposition Parameters. *Electrochimica Acta* **2021**, *367*, 137233. https://doi.org/10.1016/j.electacta.2020.137233.

(9) Svensson, J. S. E. M.; Granqvist, C. G. Electrochromism of Nickel-Based Sputtered Coatings. *Sol. Energy Mater.* **1987**, *16* (1–3), 19–26. https://doi.org/10.1016/0165-1633(87)90004-9.

(10) Makimura, Y.; Rougier, A.; Tarascon, J.-M. Cobalt and Tantalum Additions for Enhanced Electrochromic Performances of Nickel-Based Oxide Thin Films Grown by Pulsed Laser Deposition. *Appl. Surf. Sci.* **2006**, *252* (13), 4593–4598. https://doi.org/10.1016/j.apsusc.2005.07.086.

(11) Mahmoud, S. A.; Aly, S. A.; Abdel-Rahman, M.; Abdel-Hady, K. Electrochromic Characterisation of Electrochemically Deposited Nickel Oxide. *Phys. B* **2000**, *293*, 125–131.

(12) Tenent, R. C.; Gillaspie, D. T.; Miedaner, A.; Parilla, P. A.; Curtis, C. J.; Dillon, A. C. Fast-Switching Electrochromic Li+-Doped NiO Films by Ultrasonic Spray Deposition. *J. Electrochem. Soc.* **2010**, *157* (3), H318–H322.

(13) He, Y.; Li, T.; Zhong, X.; Zhou, M.; Dong, G.; Diao, X. Lattice and Electronic Structure Variations in Critical Lithium Doped Nickel Oxide Thin Film for Superior Anode Electrochromism. *Electrochimica Acta* **2019**, *316*, 143–151. https://doi.org/10.1016/j.electacta.2019.05.112.

(14) Penin, N.; Rougier, A.; Laffont, L.; Poizot, P.; Tarascon, J.-M. Improved Cyclability by Tungsten Addition in Electrochromic NiO Thin Films. *Sol. Energy Mater. Sol. Cells* **2006**, *90* (4), 422–433. https://doi.org/10.1016/j.solmat.2005.01.018.

(15) Lee, S. J.; Lee, T.-G.; Nahm, S.; Kim, D. H.; Yang, D. J.; Han, S. H. Investigation of All-Solid-State Electrochromic Devices with Durability Enhanced Tungsten-Doped Nickel Oxide as a Counter Electrode. *J. Alloys Compd.* **2020**, *815*, 152399. https://doi.org/10.1016/j.jallcom.2019.152399.

(16) Lin, F.; Nordlund, D.; Weng, T.-C.; Sokaras, D.; Jones, K. M.; Reed, R. B.; Gillaspie, D. T.; Weir, D. G. J.; Moore, R. G.; Dillon, A. C.; Richards, R. M.; Engtrakul, C. Origin of Electrochromism in High-Performing Nanocomposite Nickel Oxide. *ACS Appl. Mater. Interfaces* **2013**, *5* (9), 3643–3649. https://doi.org/10.1021/am400105y.

(17) Gillaspie, D.; Norman, A.; Tracy, C. E.; Pitts, J. R.; Lee, S.-H.; Dillon, A. Nanocomposite Counter Electrode Materials for Electrochromic Windows. *J. Electrochem. Soc.* **2010**, *157* (3), H328–H331.

(18) Ge, X.; Li, N.; Yu, X.; Cheng, J.; Chang, S.; Zhao, Q.; Cui, H.; Feng, K.; Liu, S.; Yang, X. Li2Ni(WO4)2/C: A Potential Tungstate Anode Material for Lithium Ion Batteries. *J. Alloys Compd.* **2021**, *888*, 161535. https://doi.org/10.1016/j.jallcom.2021.161535.

(19) Shruthi, D. L.; Anil Kumar, G. N.; Jagannatha Reddy, A. Luminescence and Electrical Studies of Li2Ni(WO4)2 Microcrystals. *Mater. Today Proc.* **2021**, *46*, 5772–5776. https://doi.org/10.1016/j.matpr.2021.02.713.

(20) Taylor, Z. N.; Perez, A. J.; Coca-Clemente, J. A.; Braga, F.; Drewett, N. E.; Pitcher, M. J.; Thomas, W. J.; Dyer, M. S.; Collins, C.; Zanella, M.; Johnson, T.; Day, S.; Tang, C.; Dhanak, V. R.; Claridge, J. B.; Hardwick, L. J.; Rosseinsky, M. J. Stabilization of O–O Bonds by d ^{0} Cations in Li $_{4+x}$ Ni $_{1-x}$ WO $_{6}$ ($0 \leq x \leq 0.25$) Rock Salt Oxides as the Origin of Large Voltage Hysteresis. *J. Am. Chem. Soc.* **2019**, *141* (18), 7333–7346. https://doi.org/10.1021/jacs.8b13633.

(21) Evans, R. C.; Nilsson, Z. N.; Sambur, J. B. High-Throughput Single-Nanoparticle-Level Imaging of Electrochemical Ion Insertion Reactions. *Anal. Chem.* **2019**, *91* (23), 14983–14991. https://doi.org/10.1021/acs.analchem.9b03487.

(22) Kanoufi, F. Electrochemistry and Optical Microscopy. In *Encyclopedia of Electrochemistry*; Bard, A. J., Ed.; Wiley, 2021; pp 1–80. https://doi.org/10.1002/9783527610426.bard030108.

(23) Lemineur, J.-F.; Wang, H.; Wang, W.; Kanoufi, F. Emerging Optical Microscopy Techniques for Electrochemistry. *Annu. Rev. Anal. Chem.* **2022**, *15* (1), 57–82. https://doi.org/10.1146/annurev-anchem-061020-015943.

(24) Merryweather, A. J.; Schnedermann, C.; Jacquet, Q.; Grey, C. P.; Rao, A. Operando Optical Tracking of Single-Particle Ion Dynamics in Batteries. *Nature* **2021**, *594* (7864), 522–528. https://doi.org/10.1038/s41586-021-03584-2.

(25) Pandya, R.; Valzania, L.; Dorchies, F.; Xia, F.; Hugh, J. M.; Mathieson, A.; Tan, J. H.; Parton, T. G.; De Volder, M.; Tarascon, J.-M.; Gigan, S.; de Aguiar, H. B.; Grimaud, A. Three-Dimensional Operando Optical Imaging of Single Particle and Electrolyte Heterogeneities inside Li-Ion Batteries. **2022**. https://doi.org/10.48550/ARXIV.2207.13073.

(26) Evans, R. C.; Nilsson, Z.; Balch, B.; Wang, L.; Neilson, J. R.; Weinberger, C. R.; Sambur, J. B. Quantifying Capacitive-Like and Battery-Like Charge Storage Contributions Using

Single-Nanoparticle Electro-optical Imaging. *ChemElectroChem* **2020**, *7* (3), 753–760. https://doi.org/10.1002/celc.201902011.

(27) Jiang, D.; Jiang, Y.; Li, Z.; Liu, T.; Wo, X.; Fang, Y.; Tao, N.; Wang, W.; Chen, H.-Y. Optical Imaging of Phase Transition and Li-Ion Diffusion Kinetics of Single $LiCoO_2$ Nanoparticles During Electrochemical Cycling. *J. Am. Chem. Soc.* **2017**, *139* (1), 186–192. https://doi.org/10.1021/jacs.6b08923.

(28) Jiang, D.; Sun, L.; Liu, T.; Wang, W. Thin-Film Electrochemistry of Single Prussian Blue Nanoparticles Revealed by Surface Plasmon Resonance Microscopy. *Anal. Chem.* **2017**, *89* (21), 11641–11647. https://doi.org/10.1021/acs.analchem.7b03061.

(29) Brasiliense, V.; Clausmeyer, J.; Berto, P.; Tessier, G.; Combellas, C.; Schuhmann, W.; Kanoufi, F. Monitoring Cobalt-Oxide Single Particle Electrochemistry with Subdiffraction Accuracy. *Anal. Chem.* **2018**, *90* (12), 7341–7348. https://doi.org/10.1021/acs.analchem.8b00649.

(30) Niu, B.; Jiang, W.; Jiang, B.; Lv, M.; Wang, S.; Wang, W. Determining the Depth of Surface Charging Layer of Single Prussian Blue Nanoparticles with Pseudocapacitive Behaviors. *Nat. Commun.* **2022**, *13* (1), 2316. https://doi.org/10.1038/s41467-022-30058-4.

(31) Yuan, T.; Wei, W.; Jiang, W.; Wang, W. Vertical Diffusion of Ions within Single Particles during Electrochemical Charging. *ACS Nano* **2021**, *15* (2), 3522–3528. https://doi.org/10.1021/acsnano.1c00431.

(32) Wang, J.; Toby, B. H.; Lee, P. L.; Ribaud, L.; Antao, S. M.; Kurtz, C.; Ramanathan, M.; Von Dreele, R. B.; Beno, M. A. A Dedicated Powder Diffraction Beamline at the Advanced Photon Source: Commissioning and Early Operational Results. *Rev. Sci. Instrum.* **2008**, *79* (8), 085105. https://doi.org/10.1063/1.2969260.

(33) Avdeev, M.; Hester, J. R. ECHIDNA: A Decade of High-Resolution Neutron Powder Diffraction at OPAL. *J. Appl. Crystallogr.* **2018**, *51* (6), 1597–1604. https://doi.org/10.1107/S1600576718014048.

(34) Rietveld, H. M. A Profile Refinement Method for Nuclear and Magnetic Structures. *J. Appl. Crystallogr.* **1969**, *2* (2), 65–71. https://doi.org/10.1107/S0021889869006558.

(35) Rodríguez-Carvajal, J. Recent Advances in Magnetic Structure Determination by Neutron Powder Diffraction. *Phys. B Condens. Matter* **1993**, *192* (1–2), 55–69. https://doi.org/10.1016/0921-4526(93)90108-I.

(36) La Fontaine, C.; Belin, S.; Barthe, L.; Roudenko, O.; Briois, V. ROCK: A Beamline Tailored for Catalysis and Energy-Related Materials from Ms Time Resolution to Mm

Spatial Resolution. *Synchrotron Radiat. News* **2020**, *33* (1), 20–25. https://doi.org/10.1080/08940886.2020.1701372.

(37) Ravel, B.; Newville, M. *ATHENA* , *ARTEMIS* , *HEPHAESTUS* : Data Analysis for X-Ray Absorption Spectroscopy Using *IFEFFIT*. *J. Synchrotron Radiat.* **2005**, *12* (4), 537–541. https://doi.org/10.1107/S0909049505012719.

(38) van der Walt, S.; Schönberger, J. L.; Nunez-Iglesias, J.; Boulogne, F.; Warner, J. D.; Yager, N.; Gouillart, E.; Yu, T. Scikit-Image: Image Processing in Python. *PeerJ* **2014**, *2*, e453. https://doi.org/10.7717/peerj.453.

(39) Allan, Daniel B.; Caswell, Thomas; Keim, Nathan C.; van der Wel, Casper M.; Verweij, Ruben W. Soft-Matter/Trackpy: Trackpy v0.5.0, 2021. https://doi.org/10.5281/ZENODO.4682814.

(40) Boultif, A.; Louër, D. Indexing of Powder Diffraction Patterns for Low-Symmetry Lattices by the Successive Dichotomy Method. *J. Appl. Crystallogr.* **1991**, *24* (6), 987–993. https://doi.org/10.1107/S0021889891006441.

(41) Favre-Nicolin, V.; Černý, R. *FOX* , `free Objects for Crystallography': A Modular Approach to *Ab Initio* Structure Determination from Powder Diffraction. *J. Appl. Crystallogr.* **2002**, *35* (6), 734–743. https://doi.org/10.1107/S0021889802015236.

(42) González-Platas, J.; Rodríguez-Carvajal, J. GFourier: A Windows/Linux Program to Calculate and Display Fourier Maps. Program Available within the FullProf Suite. https://www.ill.eu/sites/fullprof/php/programse811.html?pagina=Fourier (accessed 2022-09-27).

(43) Brown, I. D. VALENCE: A Program for Calculating Bond Valences. *J. Appl. Crystallogr.* **1996**, *29* (4), 479–480. https://doi.org/10.1107/S002188989600163X.

(44) Weitzel, H. Kristallstrukturverfeinerung von Wolframiten Und Columbiten. *Z. Für Krist.* **1976**, *144* (1–6), 238–258. https://doi.org/10.1524/zkri.1976.144.1-6.238.

(45) Pauling, L. THE PRINCIPLES DETERMINING THE STRUCTURE OF COMPLEX IONIC CRYSTALS. *J. Am. Chem. Soc.* **1929**, *51* (4), 1010–1026. https://doi.org/10.1021/ja01379a006.

(46) Robinson, K.; Gibbs, G. V.; Ribbe, P. H. Quadratic Elongation: A Quantitative Measure of Distortion in Coordination Polyhedra. *Science* **1971**, *172* (3983), 567–570. https://doi.org/10.1126/science.172.3983.567.

(47) Kunz, M.; Brown, I. D. Out-of-Center Distortions around Octahedrally Coordinated D0 Transition Metals. *J. Solid State Chem.* **1995**, *115* (2), 395–406. https://doi.org/10.1006/jssc.1995.1150.

(48) Kang, S. K.; Tang, H.; Albright, T. A. Structures for D0 ML6 and ML5 Complexes. *J. Am. Chem. Soc.* **1993**, *115* (5), 1971–1981. https://doi.org/10.1021/ja00058a051.

(49) Akimoto, J.; Gotoh, Y.; Oosawa, Y. Synthesis and Structure Refinement of LiCoO2Single Crystals. *J. Solid State Chem.* **1998**, *141* (1), 298–302. https://doi.org/10.1006/jssc.1998.7966.

(50) Mizushima, K.; Jones, P. C.; Wiseman, P. J.; Goodenough, J. B. (Received April 3, 1980; Communicated by J. B. Goodenough). *15* (6), 7.

(51) Ohzuku, T.; Makimura, Y. Layered Lithium Insertion Material of LiCo $_{1/3}$ Ni $_{1/3}$ Mn $_{1/3}$ O $_2$ for Lithium-Ion Batteries. *Chem. Lett.* **2001**, *30* (7), 642–643. https://doi.org/10.1246/cl.2001.642.

(52) Lu, Z.; MacNeil, D. D.; Dahn, J. R. Layered Li[Ni[Sub x]Co[Sub 1−2x]Mn[Sub x]]O[Sub 2] Cathode Materials for Lithium-Ion Batteries. *Electrochem. Solid-State Lett.* **2001**, *4* (12), A200. https://doi.org/10.1149/1.1413182.

(53) Subban, C. V.; Ati, M.; Rousse, G.; Abakumov, A. M.; Van Tendeloo, G.; Janot, R.; Tarascon, J.-M. Preparation, Structure, and Electrochemistry of Layered Polyanionic Hydroxysulfates: LiMSO $_4$ OH (M = Fe, Co, Mn) Electrodes for Li-Ion Batteries. *J. Am. Chem. Soc.* **2013**, *135* (9), 3653–3661. https://doi.org/10.1021/ja3125492.

(54) Satya Kishore, M.; Pralong, V.; Caignaert, V.; Malo, S.; Hebert, S.; Varadaraju, U. V.; Raveau, B. Topotactic Insertion of Lithium in the Layered Structure Li4VO(PO4)2: The Tunnel Structure Li5VO(PO4)2. *J. Solid State Chem.* **2008**, *181* (4), 976–982. https://doi.org/10.1016/j.jssc.2008.01.044.

(55) Ebner, W.; Fouchard, D.; Xie, L. The LiNiO2/Carbon Lithium-Ion Battery. *Solid State Ion.* **1994**, *69* (3–4), 238–256. https://doi.org/10.1016/0167-2738(94)90413-8.

(56) Meng, X.; Dou, S.; Wang, W. High Power and High Capacity Cathode Material LiNi0.5Mn0.5O2 for Advanced Lithium-Ion Batteries. *J. Power Sources* **2008**, *184* (2), 489–493. https://doi.org/10.1016/j.jpowsour.2008.04.015.

(57) Mauger, A.; Julien, C. Olivine Positive Electrodes for Li-Ion Batteries: Status and Perspectives. *Batteries* **2018**, *4* (3), 39. https://doi.org/10.3390/batteries4030039.

(58) Mauger, A.; Julien, C. M.; Armand, M.; Goodenough, J. B.; Zaghib, K. Li(Ni,Co)PO4 as Cathode Materials for Lithium Batteries: Will the Dream Come True? *Curr. Opin. Electrochem.* **2017**, *6* (1), 63–69. https://doi.org/10.1016/j.coelec.2017.10.015.

(59) Hautier, G.; Jain, A.; Ong, S. P.; Kang, B.; Moore, C.; Doe, R.; Ceder, G. Phosphates as Lithium-Ion Battery Cathodes: An Evaluation Based on High-Throughput *Ab Initio*

Calculations. *Chem. Mater.* **2011**, *23* (15), 3495–3508. https://doi.org/10.1021/cm200949v.

(60) Song, J. H.; Park, H. J.; Kim, K. J.; Jo, Y. N.; Kim, J.-S.; Jeong, Y. U.; Kim, Y. J. Electrochemical Characteristics of Lithium Vanadate, Li1+xVO2, New Anode Materials for Lithium Ion Batteries. *J. Power Sources* **2010**, *195* (18), 6157–6161. https://doi.org/10.1016/j.jpowsour.2009.12.103.

(61) Xu, K. Nonaqueous Liquid Electrolytes for Lithium-Based Rechargeable Batteries. *Chem. Rev.* **2004**, *104* (10), 4303–4418. https://doi.org/10.1021/cr030203g.

(62) Kumar, R.; Gupta, P. K.; Agrawal, A.; Nagarale, R. K.; Sharma, A. Hydrothermally Synthesized Reduced Graphene Oxide-NiWO $_4$ Nanocomposite for Lithium-Ion Battery Anode. *J. Electrochem. Soc.* **2017**, *164* (4), A785–A795. https://doi.org/10.1149/2.1181704jes.

(63) Xu, C.; Merryweather, A. J.; Pandurangi, S. S.; Lun, Z.; Hall, D. S.; Deshpande, V. S.; Fleck, N. A.; Schnedermann, C.; Rao, A.; Grey, C. P. Operando Visualization of Kinetically Induced Lithium Heterogeneities in Single-Particle Layered Ni-Rich Cathodes. *Joule* **2022**, *6* (11), 2535–2546. https://doi.org/10.1016/j.joule.2022.09.008.

(64) Zhou, H.; Xin, F.; Pei, B.; Whittingham, M. S. What Limits the Capacity of Layered Oxide Cathodes in Lithium Batteries? *ACS Energy Lett.* **2019**, *4* (8), 1902–1906. https://doi.org/10.1021/acsenergylett.9b01236.

(65) Peres, J. P.; Delmas, C.; Rougier, A.; Broussely, M.; Perton, F.; Biensan, P.; Willmann, P. The Relationship between the Composition of Lithium Nickel Oxide and the Loss of Reversibility during the First Cycle. *J. Phys. Chem. Solids* **1996**, *57* (6–8), 1057–1060. https://doi.org/10.1016/0022-3697(95)00395-9.

(66) Choi, J.; Manthiram, A. Investigation of the Irreversible Capacity Loss in the Layered LiNi[Sub 1⁄3]Mn[Sub 1⁄3]Co[Sub 1⁄3]O[Sub 2] Cathodes. *Electrochem. Solid-State Lett.* **2005**, *8* (8), C102. https://doi.org/10.1149/1.1943567.

(67) Finger, L. W.; Hazen, R. M. Crystal Structure and Compression of Ruby to 46 Kbar. *J. Appl. Phys.* **1978**, *49* (12), 5823–5826. https://doi.org/10.1063/1.324598.

(68) Ding, L.; Lee, M.; Hong, T.; Dun, Z.; Sinclair, R.; Chi, S.; Agrawal, H. K.; Choi, E. S.; Chakoumakos, B. C.; Zhou, H.; Cao, H. Noncollinear Magnetic Structure and Magnetoelectric Coupling in Buckled Honeycomb Co 4 Nb 2 O 9 : A Single-Crystal Neutron Diffraction Study. *Phys. Rev. B* **2020**, *102* (17), 174443. https://doi.org/10.1103/PhysRevB.102.174443.

(69) Newnham, R. E.; Meagher, E. P. Crystal Structure of Ni3TeO6. *Mater. Res. Bull.* **1967**, *2* (5), 549–554. https://doi.org/10.1016/0025-5408(67)90031-1.

(70) Feng, H. L.; Deng, Z.; Croft, M.; Lapidus, S. H.; Zu, R.; Gopalan, V.; Grams, C. P.; Hemberger, J.; Liu, S.; Tyson, T. A.; Frank, C. E.; Jin, C.; Walker, D.; Greenblatt, M. High-Pressure Synthesis and Ferrimagnetism of Ni_3TeO_6-Type Mn_2ScMO_6 (M = Nb, Ta). *Inorg. Chem.* **2019**, *58* (23), 15953–15961. https://doi.org/10.1021/acs.inorgchem.9b02468.

(71) Guo, H.; Fang, L.; Jiang, X.; Li, J.; Lu, F.; Li, C. A Novel Low-Firing and Low Loss Microwave Dielectric Ceramic $Li_2Mg_2W_2O_9$ with Corundum Structure. *J. Am. Ceram. Soc.* **2015**, *98* (12), 3863–3868. https://doi.org/10.1111/jace.13829.

(72) Zhao, M.-H.; Wang, W.; Han, Y.; Xu, X.; Sheng, Z.; Wang, Y.; Wu, M.; Grams, C. P.; Hemberger, J.; Walker, D.; Greenblatt, M.; Li, M.-R. Reversible Structural Transformation between Polar Polymorphs of Li_2GeTeO_6. *Inorg. Chem.* **2019**, *58* (2), 1599–1606. https://doi.org/10.1021/acs.inorgchem.8b03114.

(73) Tarakina, N. V.; Nikulina, E. A.; Hadermann, J.; Kellerman, D. G.; Tyutyunnik, A. P.; Berger, I. F.; Zubkov, V. G.; Van Tendeloo, G. Crystal Structure and Magnetic Properties of Complex Oxides Mg4−xNixNb2O9, 0⩽x⩽4. *J. Solid State Chem.* **2007**, *180* (11), 3180–3187. https://doi.org/10.1016/j.jssc.2007.09.007.

(74) Tailleur, E.; Martin, C.; Damay, F.; Fauth, F.; Maignan, A. Lack of Linear Magnetoelectric Effect in Ferrimagnetic Distorted Honeycomb $Ni_4Nb_2O_9$. *J. Appl. Phys.* **2020**, *127* (6), 063902. https://doi.org/10.1063/1.5134056.

(75) Yamane, H.; Abe, S.; Tu, R.; Goto, T. A Ramsayite-Type Oxide, $Ca_2Sn_2Al_2O_9$. *Acta Crystallogr. Sect. E Struct. Rep. Online* **2010**, *66* (10), i72–i72. https://doi.org/10.1107/S1600536810036445.

(76) Yamada, A.; Chung, S. C.; Hinokuma, K. Optimized LiFePO[Sub 4] for Lithium Battery Cathodes. *J. Electrochem. Soc.* **2001**, *148* (3), A224. https://doi.org/10.1149/1.1348257.

(77) Lin, F.; Markus, I. M.; Nordlund, D.; Weng, T.-C.; Asta, M. D.; Xin, H. L.; Doeff, M. M. Surface Reconstruction and Chemical Evolution of Stoichiometric Layered Cathode Materials for Lithium-Ion Batteries. *Nat. Commun.* **2014**, *5* (1), 3529. https://doi.org/10.1038/ncomms4529.

For Table of Contents only